Lyman-alpha forest-CMB cross-correlation and the search for the ionised baryons at high redshift

Rupert A.C. Croft[1,2⋆], A. J. Banday[2] and Lars Hernquist[3]

[1] *Dept. of Physics, Carnegie Mellon University, Pittsburgh, PA 15213, USA*
[2] *Max Planck Institute for Astrophysics, 85741 Garching, Germany*
[3] *Harvard-Smithsonian Center for Astrophysics, 60 Garden Street, Cambridge, MA 02138*

5 February 2008

ABSTRACT

The intergalactic neutral hydrogen which is responsible for the Lyα forest of quasar absorption lines is a tracer of much larger amounts of ionised hydrogen. The ionised component has yet to be detected directly, but is expected to scatter CMB photons via the Sunyaev-Zel'dovich effect. We use hydrodynamic simulations of a LambdaCDM universe to create mock quasar spectra and CMB sky maps from the same volume of space. We find that the high redshift Lyα forest gas causes temperature fluctuations of the order of 1 μK rms in the CMB on arcmin scales. The kinetic and thermal Sunyaev-Zel'dovich effects have a similar magnitude at redshift three, with the thermal effect becoming relatively weaker as expected at higher redshift. The CMB signal associated with lines of sight having HI column densities $> 10^{18} cm^{-2}$ is only marginally stronger than that for lower column density sightlines. There is a much more significant dependence of rms temperature fluctuation on mean Lyα absorbed flux, however, suggesting that the CMB signal effectively arises in lower density material. We investigate the extent to which it is possible to cross-correlate information from the Lyα forest and the microwave background to detect the Sunyaev-Zel'dovich effect at redshifts $2 - 4$. In so doing, we are enable to set direct limits on the density of diffuse ionised intergalactic baryons. We carry out a preliminary comparison at a mean redshift $z = 3$ of 3488 quasar spectra from SDSS Data Release 3 and the WMAP first year data. Assuming that the baryons are clustered as in a LambdaCDM cosmology, and have the same mean temperature, the cross-correlation yields a weak limit on the cosmic density of ionised baryons $\Omega_{b,I}$. As a fraction of the critical density, we find $\Omega_{b,I} < 0.8$ at 95% confidence. With data from upcoming CMB telescopes, we anticipate that a direct detection of the high redshift ionised IGM will soon be possible, providing an important consistency check on cosmological models.

Key words: Cosmology: observations – large-scale structure of Universe

1 INTRODUCTION

The Lyα forest seen in quasar spectra is now thought to be produced by neutral hydrogen atoms in an intergalactic medium (IGM) which is in photoionisation equilibrium (see e.g., Rauch 1998 for a review). At low to moderate redshifts, the fraction of neutral atoms is small (1 in $\sim 10^6$; e.g. Gunn & Peterson 1965) but knowledge of the photoionisation rate (from summing the contribution of known sources; e.g. Haardt & Madau 1996) makes it possible to extrapolate from this one part in a million measurement to an estimate of the total baryon density Ω_b (Weinberg et al. 1997, Rauch et al. 1997). Loeb (1996) has argued that the ionised component of the IGM should be directly observable by inverse Compton or Doppler scattering of cosmic microwave background (CMB) photons by free electrons (Sunyaev-Zel'dovich [1972,1980]; hereafter, the SZ effect). Such a detection would provide consistency checks on the currently favoured cosmological model for structure formation, and place constraints on the IGM density, temperature, ionisation state and velocity field. In this paper, we use a hydrodynamic cosmological simulation to investigate how observations of the CMB temperature and Lyα spectra of quasars drawn from the same region of sky can be used in

⋆ E-mail: rcroft@cmu.edu

the search for the hitherto unseen 99.9999% of the hydrogen associated with the Lyα forest gas at redshifts $z \approx 2 - 5$.

In favoured models for structure formation, the optical depth for Lyα forest absorption arises in a continuously fluctuating medium (e.g., Cen et al. 1994; Zhang, Anninos, & Norman 1995; Petitjean, Mücket, & Kates 1995; Hernquist et al. 1996; Katz et al. 1996a; Wadsley & Bond 1997; Theuns et al. 1998; Davé et al. 1999). The density of neutral hydrogen is inversely proportional to the photoionisation rate Γ:

$$\Gamma = \int_{\nu_{HI}}^{\infty} d\nu \frac{4\pi J(\nu)}{h\nu} \sigma_{HI}(\nu), \qquad (1)$$

and the optical depth to absorption is given by

$$\tau_{Ly\alpha} = \frac{\pi e^2}{m_e c} f \lambda H^{-1}(z) n, \qquad (2)$$

where $f = 0.416$ is the Lyα oscillator strength, n is the neutral hydrogen number density, and $\lambda = 1216$ Å (Gunn and Peterson 1965). In order for τ be of order unity, (as seen, for example at redshifts $z \sim 3$), n must be much smaller than the total density of hydrogen atoms, as noted earlier. The gas in photoionisation equilibrium lies at densities $\sim 1 - 10$ times the mean, and obeys a power law relationship between density and temperature (Gnedin & Hui 1998). At $z = 3$, according to hydrodynamic simulations (Davé et al. 2001), more than 90% of the baryons are expected to be in this diffuse component. The tiny neutral fraction is readily detectable, but not the dominant ionised portion of the material. Owing to gravitational evolution, at $z < 2$ most of the baryons are expected to reside in a shock heated IGM, with little neutral hydrogen (Cen & Ostriker 1999, Davé et al. 2001).

The interaction of CMB photons with free electrons in the intergalactic plasma was first considered by Sunyaev and Zel'dovich (1972). Inverse Compton scattering preferentially increases the energy of CMB photons, while conserving photon number, leading to a spectral distortion whose amplitude is proportional to the product of electron temperature and density (the thermal SZ effect). Doppler scattering induces an intensity fluctuation with the same spectral shape as the CMB itself (the kinetic SZ effect). The thermal effect is one of the main sources of secondary CMB anisotropies on small angular scales.

The perturbation in the CMB thermodynamic temperature resulting from scattering of nonrelativistic electrons is

$$\frac{\Delta T}{T} = y(x\frac{e^x + 1}{e^x - 1} - 4) \qquad (3)$$

$$\simeq -2y \qquad \text{for} \qquad x << 1, \qquad (4)$$

where $x = h\nu/kT_{\text{CMB}} \simeq \nu/56.85$ GHz is the dimensionless frequency and the second expression is valid in the Rayleigh-Jeans limit, which we assume henceforth. The quantity y is known as the comptonization parameter and is given by

$$y \equiv \int dl \frac{n_e k(T_e - T_{\text{CMB}})}{m_e c^2}, \qquad (5)$$

where the integral is performed along the photon path.

The kinetic SZ effect arises from the motion of ionised gas with respect to the rest frame of the CMB. The resulting temperature fluctuation is $\Delta T/T = -b$ where

$$b \equiv \sigma_T \int dl n_e \frac{v_r}{c}, \qquad (6)$$

gives the magnitude of the effect and v_r is the component of the gas peculiar velocity along the line of sight (positive sign for receding gas, negative for approaching) to the observer.

The gas which causes Lyα forest absorption has a density near the cosmic mean, with a volume weighted temperature around 2×10^4 K at $z = 3$ (e.g, Schaye et al. 2000, McDonald et al. 2001). At this temperature, we expect the contribution from the kSZ to dominate the *rms* temperature fluctuations of the CMB from the Lyα forest. Using observed Lyα forest line counts, Loeb (1996) estimated that the *rms* temperature fluctuations from the kSZ would be $\Delta T/T \sim 10^{-6}$ for the Lyα forest lying between $z = 2$ and $z = 5$. This is for angular scales of order 1 arcmin, with a θ^{-1} decrease on larger scales. There is much competition from other signals on these small scales (including low redshift thermal SZ from galaxy clusters, the Ostriker-Vishniac (1986) effect, patchy reionisation (see, e.g. McQuinn et al. 2005), and foreground sources). The suggestion to cross-correlate information from SDSS Lyα forest spectra and the CMB was also made by Loeb (1996) in order to try to better extract the signal. In this paper, we measure the kSZ effect in simulations, as well as the thermal effect. The mass weighted temperature of the IGM at $z \sim 3$ is expected to be closer to $10^6 K$ (e.g., Springel, White and Hernquist 2001), and so the thermal effect should be significant. How much of that hot gas is physically associated with Lyα absorption will affect how well the tSZ can be detected by cross-correlation.

We note that both being absorption phenomena, neither the SZ signal nor the Lyα forest opacity are directly affected by the inverse square law. The problem of finding bright QSO background sources aside, they therefore both have an advantage in the hunt for baryons at high redshifts. Indeed, the value of the SZ effect for finding galaxy clusters at the highest redshift has long been recognised (see e.g., Carlstrom et al. 2002 for a review). We aim to explore its potential for finding diffuse ionised material at $z > 2$.

The plan of this paper is as follows. In Section 2, we give details of the hydrodynamic cosmological simulation and how mock Lyα spectra and CMB temperature sky maps were constructed from the same volume of space. In Section 3, we compute statistical measures of the absorption and examine correlations between the two probes of the intergalactic medium. In Section 4, we compare directly to observational data from the SDSS and WMAP, and in Section 5 we summarise and discuss our results.

2   SIMULATED SPECTRA AND SKYMAPS

2.1   Hydrodynamic simulation

We employ a hydrodynamical simulation of the popular ΛCDM cosmology to make our prediction of the Lyα and the SZ effects. In order to both resolve the Lyα features and the bulk velocities responsible for the kSZ effect, we require a large simulation volume with good mass resolution. The data snapshots we use are from the simulation "G6", also used by Nagamine et al. (2005) to which we refer the reader for more details, which describes a representative cubic volume of space 100 h^{-1}Mpc on a side, in

a cosmological constant-dominated CDM universe, consistent with measurements from the WMAP satellite (Bennett et al. 2003, Spergel et al. 2003). The relevant parameters are $\Omega_\Lambda = 0.7$, $\Omega_m = 0.3$ $\Omega_b = 0.04$, and a Hubble constant $H_0 = 70$ km s^{-1} Mpc^{-1}. The initial linear power spectrum is cluster-normalised with a linearly extrapolated amplitude of $\sigma_8 = 0.9$ at $z = 0$. The simulation was performed with the smoothed particle hydrodynamics (SPH) code Gadget-2 (Springel et al. 2001, Springel 2005), which is based on the entropy-conserving approach of Springel & Hernquist (2002), and is an extension of the "G-series" runs of Springel & Hernquist (2003b).

The baryonic matter is initially represented by 486^3 SPH particles and the collisionless dark matter by 486^3 N-body particles. The initial mass per gas particle is therefore $9.7 \times 10^7 M_\odot$ and dark matter $6.3 \times 10^8 M_\odot$. The gravitational softening length is $5h^{-1}$kpc. The calculation includes gas dynamics, cooling, a multiphase treatment for star formation (see Springel & Hernquist 2003a), and a uniform background of ionising radiation in the manner of Katz et al. (1996b), renormalising the Haardt & Madau (1996) spectrum to reproduce the observed Lyα forest mean optical depth. A study of the SZ effect using this code was carried out by Springel, White, & Hernquist (2002), who noted that the additional physics beyond adiabatic gas dynamics had a relatively small effect; changing, for example, the mean comptonization by 20%.

2.2 Mock Lyα spectra

We use simulation outputs from redshifts $z = 2, 3, 4, 5$ and 6 to make mock Lyα spectra. For each output, this was done in the usual manner, by integrating through the SPH kernels of the particles to obtain the neutral hydrogen density field, and then convolving with the line of sight velocity field (see e.g., Hernquist et al. 1996). At each redshift, we compute 64^2 lines of sight, equally spaced on a square grid. In order to approximate longer spectra, we join together spectra after performing a random translation, reflection and choice of axis, as is done for example when making skymaps by ray-tracing through multiple copies of the simulation volume (e.g., da Silva et al. 2000). As our fiducial spectrum length, we take the distance between the Lyα and Lyβ emission lines. Later in the paper, when we cross-correlate the Lyα forest and CMB at a particular redshift, our analysis will refer to this Lyα to Lyβ region, centered on the redshift in question. For reasons of computational simplicity, we choose to ignore evolution over the length of each spectrum, both in clustering and in the mean optical depth. The Lyα to Lyβ regions correspond to comoving spatial distances of $343, 343, 330$ and 314 h^{-1}Mpc when centered on redshifts $z = 2, 3, 4$ and 5, respectively. We add partial spectra to the full spectra to ensure the correct overall length.

For each spectrum, we compute the mean effective optical depth over its entire length, i.e.,

$$\tau_{\rm eff} = -\ln\langle F \rangle, \tag{7}$$

where $\langle F \rangle$ is the mean absorbed flux in the spectrum, $\langle e^{-\tau} \rangle$. Throughout most of this paper, we will use this quantity, $\tau_{\rm eff}$, to determine the relative amount of Lyα absorption in each sightline. Another possible measure is to compute the total column density of neutral hydrogen along each sightline

from Lyα to Lyβ . Being unaffected by saturation, this will tend to reflect the presence of individual high density clouds.

As noted earlier, the simulation was run using the UV ionising background of Haardt & Madau (1996). In our subsequent analysis, we rescale the Lyα optical depths by a small amount after computing the spectra by adjusting them slightly so that $\langle F \rangle$ averaged over all spectra reproduce the observational results of Schaye et al. (2004), $\langle F \rangle = 0.878, 0.696, 0.447$ for $z = 2, 3, 4$.

2.3 CMB skymaps

At each redshift, we construct maps of the Compton y parameter and the Doppler b parameter by projecting the appropriate SPH kernel weighted quantities along one axis. Unlike Springel et al. (2001), for example, we do not project along lines which meet at a single $z = 0$ observer, as we will be interested only in the SZ signal generated by gas which falls within the same redshift interval as our Lyα forest spectra. In order to compare CMB maps and spectra for the same volume of space, we randomly translate and reflect our SZ maps in the same manner so they match up with the spectra from the previous section. We generate 40 maps, which have an angular size which subtends the whole box at each particular redshift; i.e., 94.7 arcmin at redshift $z = 2$, and 77.2, 68.5, 63.1 and 59.5 arcmin at $z = 3, 4, 5$ and 6 respectively. We make maps at a resolution corresponding to 2048^2 pixels, but also average the pixels so that we have 64^2, the same number as the Lyα spectra.

2.4 Examples

Looking at kSZ maps and Lyα spectra generated from the same region of space, we can see if there are any obvious visual relationships between the CMB temperature in pixels and the appearance of the absorption features. In Figure 1, we show the Compton y parameter, from the thermal SZ effect at $z = 2$, and alongside it five spectra which are taken with the sightline along the axis perpendicular to the plane of the map. Here, in both maps and spectra, we do not plot the entire Lyα to Lyβ region (we do this later, below), but just the material in one single cubic simulation volume. It is apparent from the map that much of the volume contributes to a very small y parameter, and that most of this redshift slice has $y < 10^{-9}$ or below. There are also a number of obvious galaxy clusters, with $y > 10^{-5}$

Of course, a map of the y parameter from all material between $z = 0$ and the last scattering surface would have quite a different appearance, with the mean y parameter being higher, of the order of 10^{-6}, and with many of the obvious filaments seen in Figure 1 washed out by projection effects. Figure 2 of White et al. (2002) demonstrates this, using a similar simulation.

Sightlines (a)-(c) in Figure 1 were chosen from those among the 64^2 we made which have large values of y. Spectrum (a) is visibly taken from near a cluster, seen in the SZ map. There, however, does not seem to be much evidence of this in Lyα absorption, at least in terms of saturated absorption. The other two spectra, (b) and (c) are also fairly similar, even though they are both associated with large y values. Because there is not much saturated absorption, we
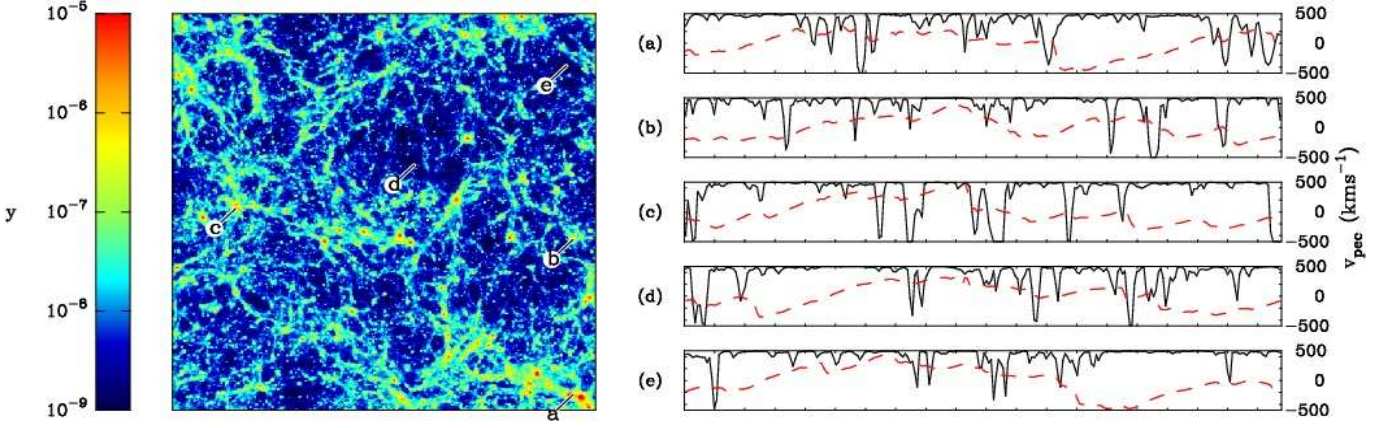
Figure 1. The tSZ CMB y parameter (left panel) for a projection of one simulation volume (side length 100 h^{-1}Mpc). We show the positions of five pixels for which we have drawn Lyα sightlines (into the page). The five spectra are shown in panels (a-e). Black curves in the right panels are the mock transmission spectra, while the dashed red curves are the peculiar velocity. Sightlines (a) and (b) and (c) have been chosen so that y is large (for (a), $y = 5 \times 10^{-6}$, for (b), $y = 1.4 \times 10^{-5}$), and for (c), $y = 3.3 \times 10^{-6}$), all among the top 1 percent of y-values. Sightlines (d) and (e) have small values of y, $y = 5.13 \times 10^{-10}$ and 3.8×10^{-10} respectively. Sightline (b) is the same as sightline (b) in Figure 2 The Lyα spectra are of length 9900 km s^{-1} (one simulation box length).
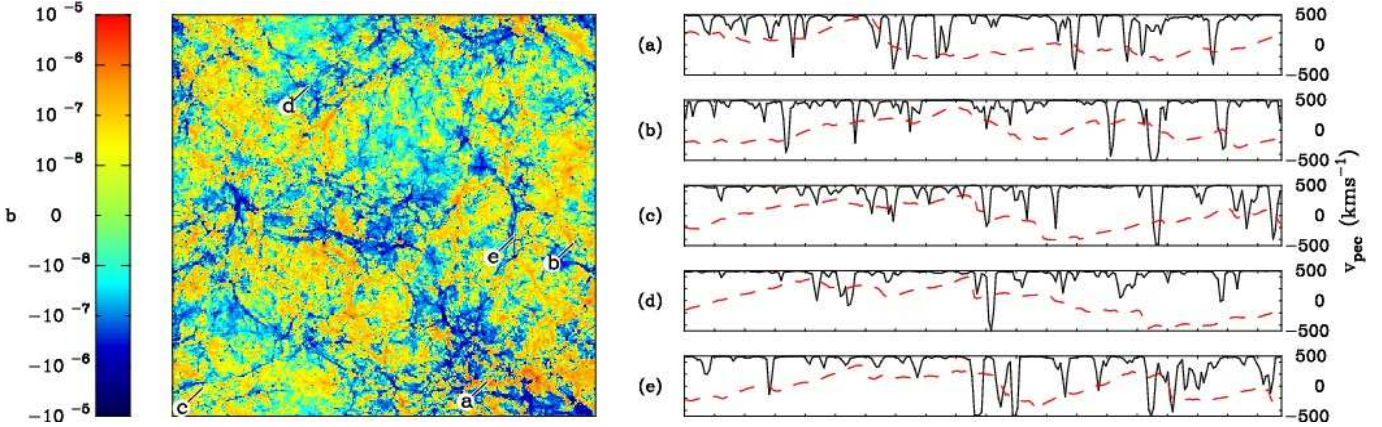
Figure 2. Projection through the simulation box showing the kSZ CMB Doppler parameter, b (left panel). Pixels with a positive values of b contain material moving on average away from the observer, and negative b values towards the observer. We show the positions of five pixels for which we have drawn Lyα sightlines (into the page). The five spectra are shown in panels (a-e). Black curves in the right panels are the mock transmission spectra, while the dashed red curves are the peculiar velocity. Sightlines (a) and (b) have been chosen so that b is large and positive (for (a), $b = 7 \times 10^{-6}$ and for (b), $b = 4 \times 10^{-6}$), both among the top 1 percent of b values. Sightline (c) is the pixel with the smallest value of $|b|$, -8×10^{-12}. Sightlines (d) and (e) have large -ve values of b, -3×10^{-6} and -6×10^{-6} respectively. The Lyα spectra are of length 9900 km s^{-1} (one simulation box length).

can see that it is unlikely that column density will correlate well with SZ decrement.

Sightlines (d) and (e) in Figure 1 have been chosen to have values of y near the bottom of the rank-ordered list of all pixels. From the SZ plot it can be seen that the spectra lie on sightlines though obvious voids, and the y values are 10000 times smaller than for panels (a)-(c). On examination, these spectra appear to have very few wide absorption features compared to spectra (a)-(c), and the overall level of Lyα absorption is slightly lower (particularly (e)).

Turning now to the map of the kSZ effect (Figure 2), we see that much of this redshift $z = 2$ slice has a Doppler $|b|$ value of $\sim 10^{-8}$, although there are several clusters and filaments dense enough and moving fast enough to reach $|b| = 10^{-5}$. Clusters can be seen moving towards the observer (blue) and away (red) . The large coherence length of

the velocity field can be seen also, from the size of the red and blue structures. Projecting the kSZ effect for a larger volume, for example subtending $z = 2 - 5$, will lead to more structures but also more cancellation of positive and negative b values. The general level of fluctuations likely agrees at least roughly with the estimate of Loeb (1996) (rms $b \sim 10^{-6}$).

Again, the kSZ plot can be compared to full lightcone maps (e.g. Figure 2 of Springel et al. 2001), which show a similar pattern of approaching and receding material, also with less obvious filamentary structure. Sightlines (a) and (b) in Figure 2 were chosen to have large positive Doppler b values, and (d) and (e) negative. It can be seen that their spectra contain fairly substantial amounts of absorption, and one can understand how the mass weighted velocity will give rise to the b values seen. Panel (c) has a velocity field

which cancels in the left and right halves of the spectrum, yielding a b parameter much closer to zero ($b \sim -10^{-11}$).

The number of sightlines passing close to galaxy groups and clusters in Figures 1 and 2 is relatively small, at least in this redshift interval. This means that any clustering statistic which weights spectra equally will tend to be sensitive to physical conditions in the regions with relatively small overdensity.

Looking at a few individual sightlines, it seems likely that there is a connection between Lyα forest absorption and SZ-induced temperature fluctuations. One way to examine this further would be to look at skymaps of both the Lyα forest and CMB. Of course, with real observations it unlikely that we would have a dense enough grid of background quasars to make a true Lyα map, but with the simulations, we can use such a technique to examine the spatial pattern of absorption. In Figure 3, we show examples of such maps, plotting the thermal and kinetic SZ effects alongside angular maps of the Lyα optical depth and column density. It should be noted that we plot the absolute value of the temperature change produced by the kinetic effect. Unlike the previous two figures, here we show a projection through the volume of space corresponding to an entire Lyα to Lyβ region (not just one simulation box). The results are centered on redshift $z = 2$, and the angular size of the maps is 95 arcmins. Because we have a grid of 64^2 Lyα spectra, we have rebinned the CMB maps so that they have the same resolution (1.5 arcmin pixels).

The grayscales of the SZ maps are the same, and so we can see from the left two panels of Figure 3 that the thermal and kinetic effects trace similar features, with the thermal effect being more prominent at this redshift. Because of the differing frequency dependence of the two SZ effects, cross-correlation of the two maps may eventually be possible using observational data, as suggested for example by da Silva et al. (2000). In the present context, we are interested in the potential cross-correlation of the Lyα forest spectra and the SZ effects. In the third panel of Figure 3, we show the mean effective optical depth, given by Equation (7) for spectra through the center of each pixel. It can clearly be seen that the patches of absorption largely follow the SZ temperature well, although there are several regions with large differences. The Lyα $\tau_{\rm eff}$ fluctuations have a somewhat lower contrast, varying by about a factor of two across the map. The obvious groups and clusters in the SZ maps do not show up as prominently in the Lyα map. This is likely to at least partly owe to the fact that regions with large amounts of Lyα absorption are saturated.

This is not the whole story, however, as we can see by looking at the rightmost panel of Figure 3. Here, we show the HI column density in each spectrum integrated from Lyα to Lyβ . There is much smaller scale structure present, as the dense knots of neutral hydrogen are picked out. The range of column densities varies from $N_{HI} = 10^{14}$ cm^{-2} to 10^{19} cm^{-2}. The structures in N_{HI} do not correlate well with the CMB maps. The smooth, large-scale structures in the SZ effect maps (and Lyα $\tau_{\rm eff}$) are not readily seen. This observation will guide our use of $\tau_{\rm eff}$ as the main Lyα statistic to be used.

In Figure 4, we show a scatter plot of the Lyα $\tau_{\rm eff}$ against the thermal SZ temperature decrement, at redshifts 2, 3 and 4, again from maps with 64^2 pixels (1.5, 1.2 and
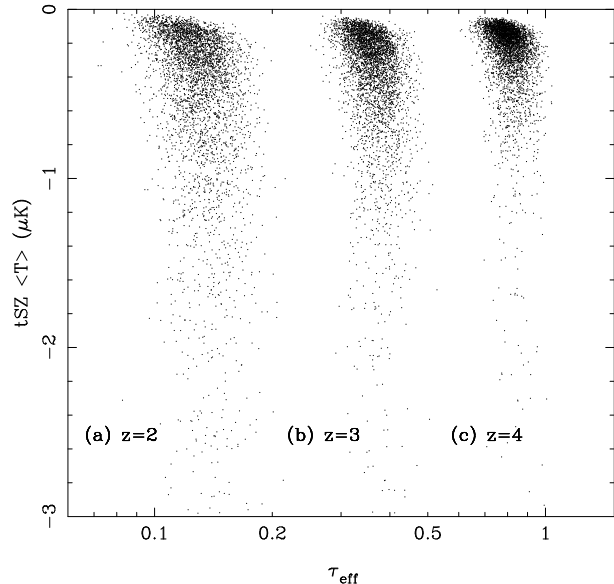
Figure 4. Thermal SZ temperature decrement T_{tSZ} vs Lyα forest $\tau_{\rm eff}$ for spectra at three different redshifts.

1.1 arcmin size for z=2,3,4). The correlation between the two quantities is apparent, and in particular at each redshift there are few lines of sight with very low values of $\tau_{\rm eff}$ but substantial SZ decrements. There is a large amount of scatter, however, indicating that even if foreground/background noise is not an issue, it will be necessary to average over many sightlines to obtain statistically significant results.

3 STATISTICAL MEASURES

In this section, we use the set of skymaps and spectra generated from our simulation to examine statistically the CMB fluctuations caused by Lyα forest gas.
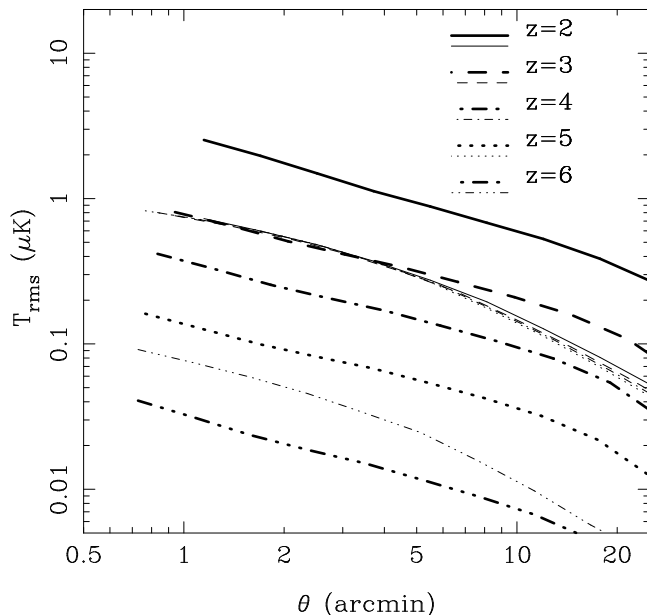
3.1 Rms temperature fluctuations

In Figure 5, we show the rms temperature fluctuations averaged in top-hat circles on the plane of the sky, calculated from maps such as those shown in the left two panels of Figure 3. We show results centered on integer redshifts between $z = 2$ and $z = 6$, in each case, calculating only the CMB fluctuations caused by gas within the Lyα to Lyβ region of the spectrum. The thermal and kinetic SZ effects are shown separately, and it can be seen that at $z = 2$, T_{rms} is approximately three times larger for the tSZ effect, as we expect from Figure 3. At $\theta = 1$ arcmin, the rms T fluctuations are $\sim 2\mu$K for the tSZ at this redshift.

The curves for all redshifts have an angular dependence given by $\sim \theta^{0.6}$. At $z = 3$, the two SZ effects are comparable, and beyond that the kSZ effect stays approximately constant out to $z = 5$. The rms peculiar velocity of the gas increases slightly with decreasing redshift, as detailed in Table 1. This is balanced by the decrease in angular size for a given comoving length which shifts the curves to the left. The main change in the kSZ at $z = 6$ is caused by the switching on of the UV ionising background in our model, and so the ionised fraction is small then. The temperature of
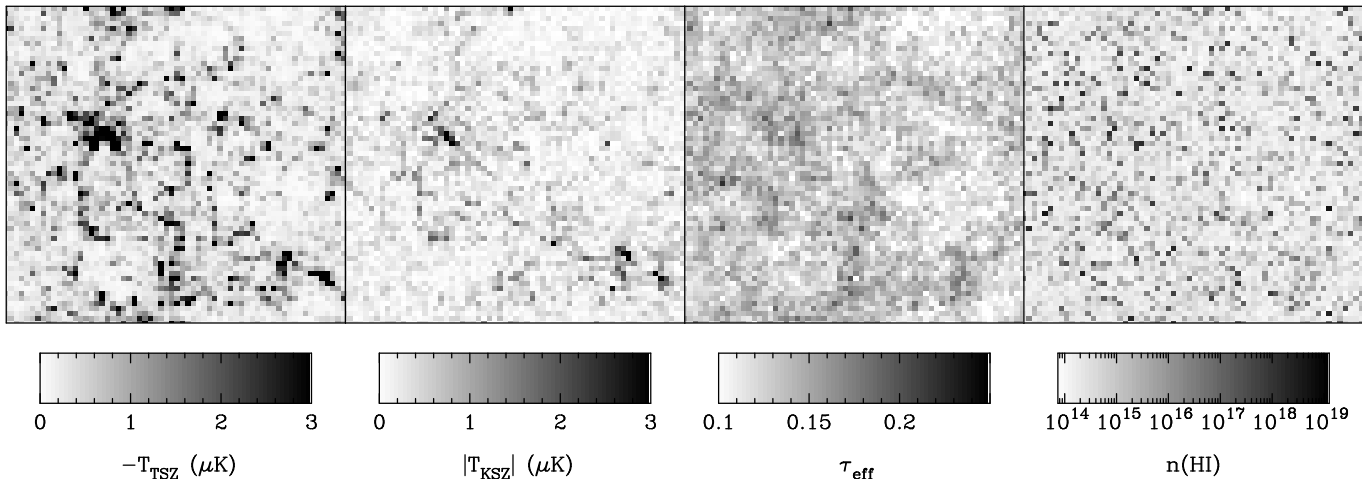
Figure 3. Sky maps of CMB temperature (left panel) owing to the kSZ effect at z=2 (for a volume equivalent to the entire Lyα to Lyβ spectral width). The width of the panel is 95 arcmin. We also show |T|, mean flux < F > in Lyα spectra and total column density in Lyα spectra. In each map, there are 64 × 64 pixels.

Figure 5. Rms CMB temperature fluctuations in top-hat circles as a function of radius (x-axis) for three different redshifts. In each case, we plot the rms fluctuations associated with a volume which would contain material with HI absorption wavelengths from Lyα to Lyβ centered on the indicated redshift. Thin lines are kinetic SZ and thick lines thermal SZ.

Table 1. The mass density and electron number weighted gas temperature and velocity dispersion in the simulation at different redshifts.

z	T_ρ (K)	T_e (K)	$v_{rms,\rho}$ (km s^{-1})	$v_{rms,e}$ (km s^{-1})
6	7.1×10^3	1.9×10^5	136	166
5	2.57×10^4	2.60×10^4	149	148
4	6.86×10^4	6.89×10^4	164	164
3	1.77×10^5	1.76×10^5	185	185
2	5.04×10^5	5.04×10^5	214	214

increases the temperature by another factor of 20 by $z = 2$. The rise in T_{rms} owes mostly to this, with a small part coming from the factor 2.3 increase in linear density fluctuations themselves between the two redshifts.

We note that although the thermal SZ effect is dominant at redshifts $z < 3$, the signal that is actually generated in gas that directly produces the Lyα forest is a small fraction of the total thermal SZ signal at that redshift. This is because the temperature of Lyα forest-producing gas at the mean density at $z = 3$ is $\sim 10^4$K, low enough that the thermal SZ effect should be extremely small (e.g., Loeb 1996). The thermal SZ signal we are instead seeing is largely generated in the Warm-Hot Intergalactic Medium (WHIM, e.g. Davé et al. 2001) at these redshifts which is collisionally ionised, and is responsible for the higher mass-weighted temperature seen in Table 1. As we discuss below, the thermal SZ signal at this redshift is strongly correlated with the Lyα absorption signal, indicating that the WHIM signatures are physically associated with the same large-scale structures as the Lyα forest, tracing their higher density regions.

3.2 Cross-correlation function

We have seen that IGM gas at redshifts $z = 2$ to $z = 5$ yields rms CMB temperature fluctuations on the order of a few μK. One could calculate the angular power spectrum, the C_ls, and then see whether it could be separated from

the gas influences the fluctuations owing to the thermal effect directly, and this has a much more rapid dependence on redshift. In Table 1, we can see that at $z = 6$, the electron-weighted mean temperature is $> 10^5 K$, as the free electrons are concentrated in the few collisionally ionised structures present at that redshift.[1] By $z = 5$ when most of the IGM is photoionised, the electron-weighted temperature is 2.6×10^4 K, and as gravitational evolution continues, shock heating

---

[1] We ignore any difference between the electron and ion temperatures; see Yoshida et al. (2005).
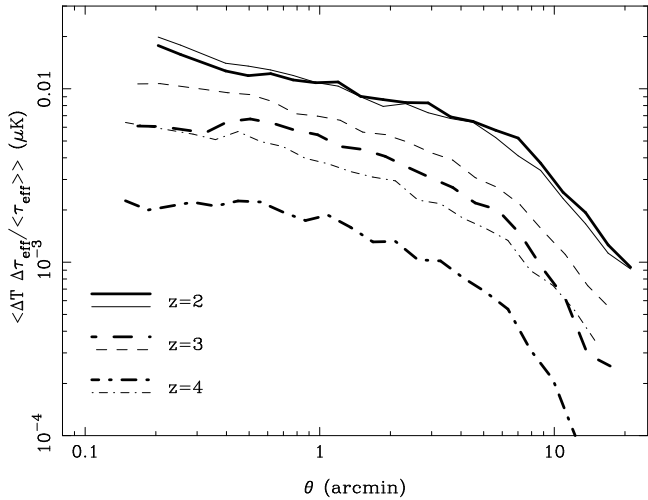
Figure 6. Cross-correlation of $|T|$ (for kSZ) or T (for tSZ) and $F/<F>$ as a function of pixel-pixel distance, for three different redshifts. Results for tSZ are shown by thick lines and kSZ by thin lines.

other small angle fluctuations. Owing to the multitude of other possible signals, however, it is likely to be more useful to cross-correlate with material at a known redshift, and use this to extract information. As the Lyα forest contains most of the baryons at these redshifts, and the mean effective Lyα optical depth appears to correlate visually with CMB temperature in Figure 3, we use this quantity in our cross-correlation.

We compute the cross-correlation separately for the tSZ and kSZ effects. For the kSZ, because the magnitude of the effect can be positive of negative, we work with $|T_{tSZ}|$. Although this is not easily done with observational data, in the current section we are interested in making a relative comparison between the magnitude of the tSZ and kSZ effects, where this is a useful approach. In order to do the cross-correlation, for each Lyα spectrum we first calculate $\Delta\tau_{eff} = -(\tau_{eff} - \langle\tau_{eff}\rangle)/\langle\tau_{eff}\rangle$, where $\langle\tau_{eff}\rangle = -\ln\langle F\rangle$ and we use the average mean transmitted flux for all spectra. The cross-correlation we compute is $\langle\Delta\tau_{eff}\Delta T\rangle$, which has units of μK. For the kSZ we use $\Delta T = |T| - \langle|T|\rangle$ and for the tSZ, $\Delta T = T - \langle T\rangle = T$. The results for redshifts $z = 2 - 4$ are shown in Figure 6. We have not rebinned the CMB temperatures to the angular resolution of the spectrum grid, so that we are able to show results down to angular scales below 1 arcmin.

Unlike the case for the rms T fluctuations, one can see that the cross-correlation statistic for the kSZ effect depends on redshift, driven by evolution in the Lyα forest. On first inspection, this is somewhat puzzling, as Lyα τ_{eff} fluctuations should be increasing towards high redshift, as the mean optical depth increases, but instead they are smaller. This is because we have divided out $\langle\tau_{eff}\rangle$, and so the fractional fluctuations are indeed smaller. Measurements based on the flux F, instead divide out $\langle F\rangle$ which is smaller at high redshift (see e.g., Croft et al. 1998).

This statistic and its spatial dependence could in principle be measured observationally for the thermal SZ effect. We will return to this point in Section 5.

3.3 One dimensional distributions

We have seen from Figure 4 that there is a dependence of SZ decrement and the Lyα τ_{eff} for spectra in the same pixel. We will average this relationship over many pixels and bin as a function of τ_{eff}, in order to visualise the mean trend of T vs τ_{eff}. This simple statistic is one which we will concentrate on in this subsection, and use in Section 4 below to compare to observational data. The mean trend of T vs τ_{eff} does depend on the resolution of the CMB map, and we present results for the same resolution as the spectrum grid (64^2 pixels, each of width 1.2 arcmin at z=3) as well as smoothing with a Gaussian filter with FWHM 13 arcmin (the WMAP W-band resolution, see Bennett et al. 2003). We will also plot the rms temperature fluctuations in pixels caused by the kinetic SZ effect.

Figure 7 shows our results for three different redshifts, with the top panels being the tSZ decrement. We can see that the overall level of the temperature decrement is strongest for $z = 2$ and weakest for $z = 4$, as expected. At $z = 2$, pixels with Lyα τ_{eff} =0.07 have tSZ temperature decrements of $\sim 0\mu$K, and the pixels with τ_{eff} =0.2 have decrements $\sim -1.5\mu$K. Between these two extremes, the trend of T with τ_{eff} is close to linear. The Lyα spectra with the very highest levels of absorption, $\tau_{eff} \gtrsim 0.2$, exhibit a weakening of the decrement, likely owing to radiative cooling of the gas in these high density regions producing relatively more neutral hydrogen. The signal smoothed at the WMAP resolution is somewhat weaker, but still easily measurable from the simulations.

In the middle panels of Figure 7, we show the kSZ induced rms temperature fluctuations. They exhibit a rise with increasing τ_{eff}, in accord with the rise in density probed by the sightlines, again with a turndown for the spectra with the very highest absorption levels. As with the rms in circles plotted in Figure 5, the level of fluctuations changes little with redshift. Smoothing the map to the WMAP resolution does affect the level strongly, however, reducing the magnitude of the signal by roughly a factor of ten. As rms fluctuations are already more difficult to measure in the presence of noise than the mean level, this means that it is likely that the thermal rather the kinetic SZ effect will be easiest to target when considering the analysis of observational data.

One can ask whether the signal from the tSZ and kSZ effects arises in low or high density gas, and whether we are really sampling the low density IGM probed by the Lyα forest. Because our measure of the τ_{eff} - T correlation is angular pixel weighted (we are using a histogram of pixel values), the fact that most of the sightlines we use will contain relatively little gas comes into play. For example, only a few of the pixels in Figure 3 pass close to clusters and groups, and most of the spectra with the lowest 90 percent of τ_{eff} values are likely to pass through only void-like regions in the Lyα to Lyβ interval. This means that while the thermal SZ does directly probe the mass weighted (or rather electron number-weighted) IGM temperature, and so is dominated by virialised objects, by breaking up the signal as a function of τ_{eff} we introduce sensitivity to what is occurring in low density regions.

In Figure 3, we saw that there appeared to be a much better correspondence between CMB temperature and τ_{eff} than HI column density. Nevertheless, from looking at the
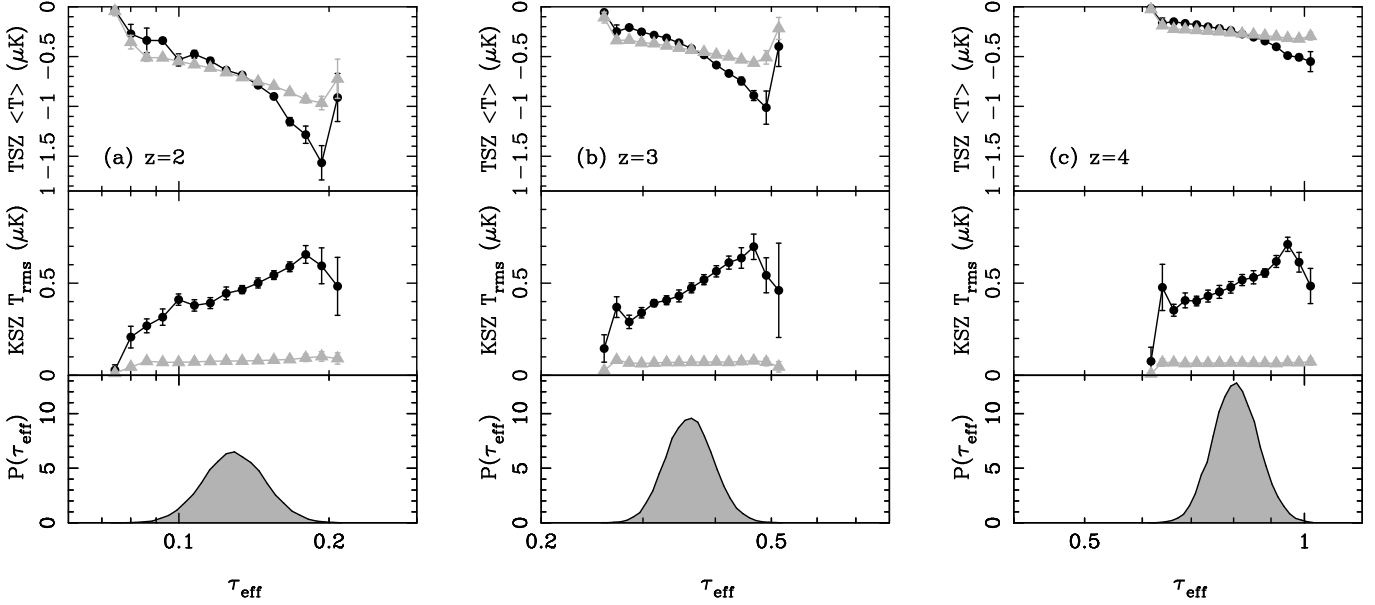
Figure 7. Top panels: Dependence of mean temperature from the thermal SZ effect on $\tau_{\text{eff}} = -\log < F >$ for spectra running through the pixels. Middle panels: Dependence of rms temperature fluctuation in pixels (1.5, 1.2 and 1.1 arcmin size for z=2,3,4) on $\tau_{\text{eff}} = -\log < F >$ for spectra running through the pixels, for three different redshifts (left to right). The round symbols which make up the upper curve in each case show results for pixels, unsmoothed, and the triangles for maps smoothed with a Gaussian filter of FWHM 13 arcmins, similar to the WMAP W-band resolution. Error bars are from the scatter between 10 fields in each case (size 95, 77, 69 arcmin for $z = 2, 3, 4$). Bottom panels: the pdf of $\tau_{\text{eff}} = -\log < F >$ for spectra from Lyα to Lyβ.
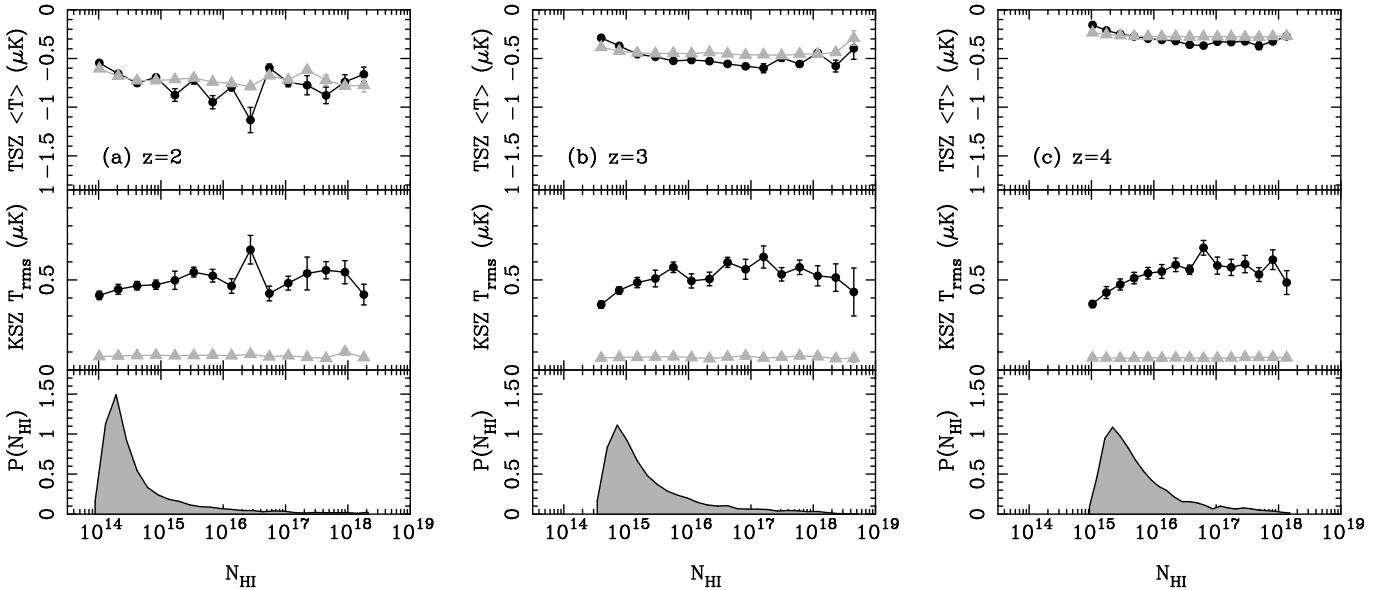

Figure 8. Top panels: Dependence of rms temperature fluctuation in pixels (same size as Figure 7) on NHI for spectra running through the pixels, for three different redshifts (left to right). The round symbols which make up the upper curve in each case show results for pixels, unsmoothed, and the triangles for maps smoothed with a Gaussian filter of FWHM 13 arcmins, similar to the resolution of the WMAP satellite. Error bars are from the scatter between 10 fields in each case (size 95, 77, 69 arcmin for $z = 2, 3, 4$). Bottom panels: the pdf of NHI for spectra from Lyα to Lyβ.

maps it was not immediately obvious that the very highest density objects are in fact associated with large amounts of HI and have a significant SZ signal. In Figure 8 we plot CMB T vs N_{HI}, and see that there is a slight increase in the SZ signal for sightlines with $N_{HI} = 10^{14} - 10^{16}$ cm^{-2}, for all redshifts. The curves, however, are relatively flat at

higher column densities. It appears that information from saturated regions will not be helpful in carrying out Lyα forest CMB correlations, and so there is little need for high resolution spectra. In order to shed further light on this, in Figure 9 we have plotted values of N_{HI} vs τ_{eff} for individual sightlines, as a scatter plot (as always, we average over the
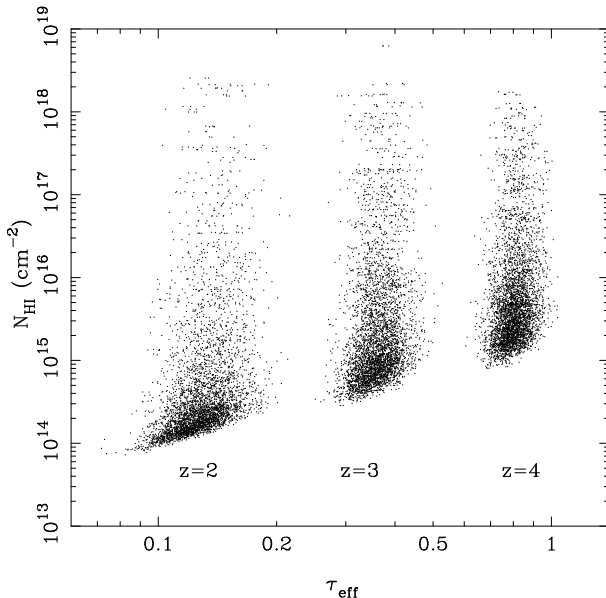
Figure 9. $N_{\rm HI}$ vs $\tau_{\rm eff}$ for spectra at three different redshifts.

Lyα to Lyβ region in each spectrum). We expect there to be an envelope, a minimum N_{HI} for sightlines with a given $\tau_{\rm eff}$. This minimum level would correspond to a uniform distribution of absorbing material (see e.g., Weinberg et al. 1997). We can see such an envelope, but also a large scatter towards higher values of N_{HI}. The fractional scatter in N_{HI} increases for larger $\tau_{\rm eff}$, so it is not surprising that for high $\tau_{\rm eff}$ there is little evidence of a trend in Figure 8.

4 LIMITS FROM SDSS AND WMAP DATA

4.1 Method

The microKelvin fluctuations produced by the Lyα forest gas are likely too small to be detected directly in current data (e.g., Bennett et al. 2003, Kuo et al. 2004). However, it is possible that by comparing observational statistics with simulation results we can come up with interesting limits on the population of ionised baryons, as well as estimating the properties of the observations necessary to make a direct detection. Based on our investigations in the previous sections, a good strategy will be to measure $\tau_{\rm eff}$ for the Lyα forest as well as the CMB temperature in pixels where there are Lyα spectra. For the present limited observational study, we choose to investigate the one-dimensional distributions of these statistics, as in Section 3.3. We do this for reasons of simplicity, and because breaking up the signal into sightlines with high and low absorption levels will enable us to look for an obvious distinct signature (unlike a full spatial cross-correlation analysis which would have more discriminating power, but be more difficult to interpret).

In our analysis, we calculate the mean and rms CMB temperature for pixels binned using the $\tau_{\rm eff}$ of the spectra that pass through them. We use a jackknife estimator (e.g., Bradley 1982) to compute the error bars, breaking up the data into 50 subsamples. We have also computed error bars by randomly rotating the CMB data with respect to the Lyα forest data and find them to be broadly consistent.

4.2 Lyα forest data

We use the Lyα forest of quasar spectra taken from Data Release 3 of the Sloan Digital Sky Survey (Abazajian et al. 2005). Our data sample consists of 3488 quasar spectra with quasar redshifts greater than 2.4, pruned to remove Broad Absorption Line quasars. The particular dataset was compiled from the publically available data by Scott Burles and kindly made available to us (Burles, private communication). Owing to the relatively high low-redshift limit for the quasars, the spectra consist of the full Lyα to Lyβ region of the forest, lying above the atmospheric cutoff at ~ 3200 Å . This will be useful in order to be consistent with what was done in the simulations.

The one-dimensional distribution of $\tau_{\rm eff}$ requires that the data be divided into broad bins (we will use five bins). In order to calculate $\tau_{\rm eff}$ for each spectrum, we need to fit the continuum over the full Lyα to Lyβ region. Historically, the averaged value of the mean transmitted flux from many spectra has been used to calculate a global value of $\tau_{\rm eff}$ (e.g., Kirkman et al. 2005). Fluctuations in $\tau_{\rm eff}$ for entire spectra have not been estimated, however, presumably owing to problems with calculating a mean value on large scales where continuum fluctuations are seen to be comparable to fluctuations in the absorption (see for example the power spectrum of the raw spectrum in Hui et al. [2001] or McDonald et al. [2004]). The largest scale on which fluctuations intrinsic to the Lyα forest have been measured is 153 Mpc at redshift $z = 1.9$ by Tytler et al. (2004), who find that Lyman limit systems and metal lines make large contributions to fluctuations in the mean flux at this relatively low redshift. In our case, we will be working at $z = 3$, where these effects should be less important. Nevertheless, we expect that there will be a large contribution to the variation in $\tau_{\rm eff}$ from sightline to sightline owing to continuum estimate errors as well as noise in the spectra and non-Lyα absorption. We leave the question of how best to fit the continuum on the largest scales to other work (e.g., Suzuki et al. 2005), and in the meantime, we will add a Gaussian distribution of errors to our simulation measurement to account for these effects when comparing our simulations with observations. The relatively large bin size should serve to mitigate effects of $\tau_{\rm eff}$ errors in this first illustrative comparison.

We fit the continuum using the often employed polynomial fitting method (e.g., Croft et al. 1998). A low order polynomial (3rd order in our case) is fit to the Lyα forest region. We avoid the Lyα and Lyβ emission lines by restricting our fit to the rest wavelength range 1030-1190Å. We then remove all points more than 2 σ below the continuum and refit, iterating this procedure until convergence is achieved. Averaging over all Lyα pixels in our dataset, we find a mean redshift $z = 2.91$. At this stage we divide out the continuum and compute a value of F. For all spectra, we find $F = 0.8$. Measurements of the mean flux and global value of $\tau_{\rm eff}$ from higher resolution datasets better suited to this measurement find a lower value of F (e.g., Schaye et al. 2004, Kirkman et al. 2005). Our measurement of F is on average biased high because we miss absorption in flatter low density regions around the continuum owing to our low resolution. We correct for this bias in a crude way by multiplying the value of the fit continuum in each case by 1/0.85. This simple correction is adequate for our current purposes,
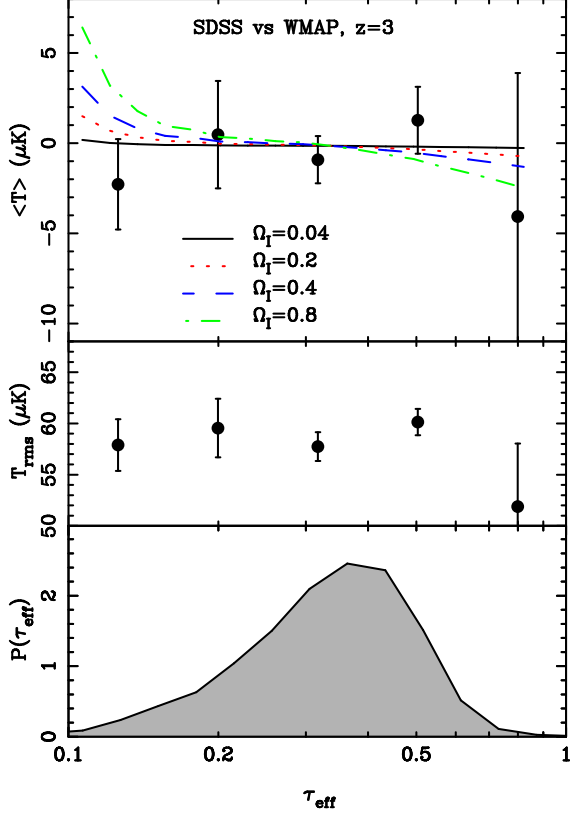
Figure 10. SDSS $\tau_{\rm eff}$ vs WMAP T for $z = 3$. We show jackknife errors (10 subsamples). We have subtracted off a ring for background from 15-25 arcmin around the pixel that the spectrum is in. The lines show predictions from LCDM after broadening the $\tau_{\rm eff}$ values with observational errors. The solid line is for the LCDM baryon density, dotted for LCDM $\times$ 5 (i.e. $\Omega_{b,I} = 0.4$) and dash-dotted LCDM $\times$ 20 (i.e. $\Omega_{b,I} = 0.8$).

having been set so that we reproduce the global $\tau_{\rm eff}$ value of Schaye et al. (2004) at $z = 3$. We make the assumption that any random variations in this bias from spectrum to spectrum will simply act as an additional source of noise which we can model in our simulation data.

In the bottom panel of Figure 10 we have plotted a histogram of the $\tau_{\rm eff}$ values derived from the SDSS spectra. The mode of the distribution is $\tau_{\rm eff}$ =0.35, the same as the simulation results at $z = 3$ plotted in Figure 7. In the observational data, there is a tail extending down to $\tau_{\rm eff} \sim 0.1$ and up to $\tau_{\rm eff} \sim 1$ which owes to noise and the continuum fitting uncertainties described above.

4.3 CMB data

We make use of the WMAP first year data (Bennett et al. 2003) in our analysis. For the illustrative application of Lyα-CMB cross-correlation in this paper, we employ the foreground cleaned version of the data presented by Tegmark et al. (2004). The CMB temperature is given in HEALPix format (12×512^2) pixels, at the resolution of the WMAP W-band data (13 arcsec FWHM).

The Tegmark et al. map is chosen by us because it combines the 5 WMAP channels into a map with the highest angular resolution possible. However, because it is de-

rived from channels with different frequencies and the thermal SZ effect has a weak frequency dependence, the map will have a scaled value of the SZ effect present, dependent on the weights used to combine the channels. In order to understand what impact this will have, we can use Equation 3 to examine the thermal SZ temperature fluctuations in the different bands. Equation 3 can be written in the form $\Delta T/T = f(\nu) \times y$, and at the lowest frequencies, $f(\nu) \to -2.0$. The five WMAP channels are centered at frequencies of 23, 33, 41, 61 and 94 GHz. The values of $f(\nu)$ for the channels are then $-1.97, -1.94, -1.91, -1.81$ and -1.56, respectively. The weights for the Tegmark map vary spatially and are not publically available, but one can see the maximum difference of the effect compared to our Rayleigh Jeans approximation ($f(\nu) = -2.0$) by considering the 94 GHz W-band map on its own, which gives approximately a 22% reduction in the predicted tSZ signal. If we instead assume that the weights will have a similar effect to those used by the WMAP team itself for their linearly combined map, we find by summing over the 5 bands that $f_{\rm effective} = \sum_i^5 W_i f_i(\nu) = -1.79$, or a $\sim 10\%$ reduction, The effect of frequency dependence is therefore small enough and uncertain enough that we neglect it in our illustrative application to observational data. In the future, however, as we have mentioned before, the frequency dependence can be used to better extract the signal. We will return to this point.

For each pixel centered on one of the SDSS quasar spectra, we extract the corresponding CMB temperature of that pixel. In order to crudely mitigate the effects of primary CMB anisotropies, which act as noise for our signal, we subtract a local background consisting of the CMB temperature averaged over all pixels in an annulus of inner radius 15 arcmin and outer radius 25 arcmin, centered on the pixel in question. Our motivation for this background subtraction is the fact that the SZ signals fall off rapidly on large scales (e.g. see Figure 6), unlike the CMB primary signal. Because we will only be computing an upper limit to the SZ signal, this subtraction is a conservative assumption.

The presence of CMB primordial anisotropies will produce fluctuations on large scales. For example, there will be coherent fluctuations on the 100 arcmin scales which our simulated sky maps cover. The annulus subtraction technique represents a crude way to deal with this. As we shall see below, the noise level on the pixel scale is sufficiently large with the WMAP data that we are not limited by the primary fluctuations in our analysis. However, in the future, with better data it will become imperative to model and remove the effect of the primordial anisotropies. This could be done with matched filtering (e.g., Schaefer et al. 2004), and the technique tested with simulations of the CMB sky which include large-scale anisotropy, foregrounds, noise and an instrumental beam response. We leave this for future work, and in Section 5.2 we will discuss other more sophisticated ways to deal with the CMB data.

4.4 Results

We find the rms temperature fluctuations in all 3488 pixels containing spectra to be 60μK. In the middle panel of Figure 10 we show the rms temperature in each of 5 $\tau_{\rm eff}$ bins. The error bars range from 1.3 to 6.1μ K. This is close to the

Poisson error estimate in each case, which is not surprising because the pixels are sampled quite sparsely from the data. Given that we expect $\sim 1\mu K$ rms fluctuations at most from the kinetic SZ effect, it is clear that this particular dataset will fall short of giving us any meaningful constraint from the kSZ. Because the kSZ signal will add in quadrature to the rms from the noise and CMB primary signal, the highest τ_{eff} bin might have a total rms of $\sqrt{60^2 + 1^2}\mu K$ and the lowest $\sqrt{60^2 - 1^2}\mu K$, a difference of 0.02 μK. In practice, because the CMB data is smoothed, we expect at least a factor of 10 less signal (see the middle panel Figure 7). The kSZ signal is therefore at least 500 times too small to be detectable in this way with these data.

If instead we turn to the thermal SZ signal, the situation is much more promising. As a mean temperature rather than a variance, it is easier to constrain this signal from noisy data. In the top panel of Figure 10 we show the mean temperature in pixels for the 5 bins of Lyα τ_{eff} . Owing to the background subtraction, the mean value of the pixels is zero. When comparing to the simulation data, we will renormalise so that the same is true. The observational error bars vary from 1.3 to 8.0 μK per bin.

From Figure 7, we expect the mean temperature decrement from the thermal SZ effect at redshift $z = 3$ to exhibit a total variation of $\sim 0.6\mu K$ amongst the pixels with highest and lowest Lyα forest τ_{eff} . This is for CMB maps at the WMAP resolution, but unfortunately not including noise in the Lyα τ_{eff} estimates. As detailed in Section 4.2 above, we model the effects of noise in the spectra and continuum fitting uncertainties by adding a Gaussian-distributed error to the τ_{eff} from simulations. We add a τ_{eff} value randomly drawn from a normal distribution with standard deviation $\sigma = 0.1$. Doing this to the simulated values of τ_{eff} enables us to reproduce the width of the histogram of observed τ_{eff} values. In the top panel of Figure 10 we plot the curve of simulation CMB temperature $\langle T \rangle$ vs. simulated τ_{eff} after this noise has been added. The line which lies closest to the $\langle T \rangle = 0$ axis is this prediction. As we can see, the predicted variation of $\langle T \rangle$ with τ_{eff} is barely noticeable on this scale, indicating that tight constraints lie only in the future with larger observational datasets.

Nevertheless, the comparison is interesting because it constitutes an attempt to detect the ionised baryons at $z = 3$, and the sensitivity increase required for success if our current cosmological models are correct is only about one order of magnitude. In order to place an upper limit on the temperature and density of ionised baryons using existing data, one would ideally use a grid of simulations with different values of the baryon density, with the amplitude of matter fluctuations normalised so that their clustering and other properties are consistent with observations (e.g. Spergel et al. 2003, Tegmark et al. 2004). In this manner, both the clustering of baryons and the variation of mean IGM temperature with Ω_b could be marginalised over to yield a constraint on Ω_b from ionised baryons, $\Omega_{\mathrm{b,I}}$. The effects of varying Ω_b on structure at high redshift were explored with a suite of simulations by Gardner et al. (2003). These authors found for example that Lyα forest absorption is virtually unaffected by changing Ω_b (by a factor ~ 6), as long as the ionising background intensity is adjusted to reproduce the same value of τ_{eff} .

In the present case, because of the large error bars, the

value of $\Omega_{\mathrm{b,I}}$ consistent with observations is likely to be so high that a simpler and more crude approach than a full simulation grid is all that is warranted. In order to model the effect of increasing Ω_b we simply multiply the simulation value of SZ $\langle T \rangle$ by a constant factor, assumed to be equivalent to multiplying Ω_b by the same factor. We do not adjust the Lyα observables, imagining that any increase in baryon density can be cancelled out by the presence of a UV background radiation field higher in intensity by the same factor. Moreover, we assume that increasing Ω_b does not affect the amplitude of matter fluctuations and that the temperature of the IGM stays the same as in the $\Omega_b = 0.04$ simulation. A model with a very large value of Ω_b is likely to have many other differences related to gas physics and cooling, such as the number of collapsed baryonic objects. Additionally, of course, it will be incompatible with Big Bang Nucleosynthesis constraints (e.g., Burles and Tytler 1998), and measurements of Ω_b from the CMB acoustic peaks (Spergel et al. 2003). None of these problems concern us here, as our comparison to simulations is essentially illustrative.

Under these assumptions, a χ^2 fit of the simulation data to the WMAP/SDSS data, both binned in the same manner, yields $\Omega_{\mathrm{b,I}} < 0.55$ at 90% confidence and $\Omega_{\mathrm{b,I}} < 0.80$ at 95% confidence. The limits on the fraction of the critical density in ionised baryons at $z = 3$ are therefore very weak. This is as one would expect from looking at Figure 10 where we show the simulation curves for various values of $\Omega_{\mathrm{b,I}}$. It is possible to conclude that the Universe is not closed by ionised baryons, but not much else. This situation is likely to be much improved with future observational data, as we will discuss below.

Much of the statistical power in the measurement comes from the bin with the lowest value of τ_{eff} . Most of the pixels have moderate values of τ_{eff} but these pixels in the lowest bin also have low SZ decrement amplitudes. In this manner, the CMB-Lyα forest cross-correlation can be said to be probing the low density IGM.

5   SUMMARY AND DISCUSSION

5.1   Summary

Using a cosmological hydrodynamic simulation we have investigated the CMB temperature fluctuations caused by the diffuse IGM at redshifts $z = 2 - 6$, also responsible for the Lyα forest. Our main findings can be summarised as follows:

(1) At redshift $z = 2$, the kinetic Sunyaev-Zel'dovich effect from gas within the Lyα to Lyβ region of the forest is predicted to cause CMB fluctuations of amplitude 0.8 μK rms averaged in a top-hat filter of angular radius 1 arcmin. This remains roughly constant for higher redshifts.

(2) The thermal SZ at redshift $z = 2$ yields an rms T of 2.4 μK. At higher redshift, the relative fluctuation owing to the thermal SZ compared to kinetic SZ declines as expected because of the decreasing mean temperature. However, there is still a substantial T_{rms} at higher redshift, 0.4 μK at $z = 4$.

(3) There is a correlation between Lyα forest properties of quasar spectra with CMB temperature fluctuations

caused by both the kinetic and thermal SZ effects. In particular, there is a strong relation between the mean effective optical depth τ_{eff} averaged over the entire Lyα forest region and the CMB temperature. Pixels (of size ~ 1 arcmin) in the top 10 percentile of τ_{eff} are predicted to have a mean CMB temperature 1.5 μK lower than the bottom 10 percentile at $z = 2$, owing to the thermal SZ effect. The quantity τ_{eff} is relatively sensitive to density fluctuations in the diffuse IGM.

(4) There is, however, little correlation between the total HI column density in spectra and the CMB temperature, with no relation at all seen for column densities $N_{HI} > 10^{16} cm^{-2}$. This statistic is most sensitive to the neutral hydrogen density in saturated regions, indicating that SZ effects correlate best with relatively diffuse unsaturated gas.

(5) We have compared the correlation of Lyα τ_{eff} with CMB T seen in simulations of the ΛCDM cosmology with observational data from the Sloan Digital Sky Survey and WMAP. Because the kinetic SZ signal and pixel noise add in quadrature, no constraints are possible on the IGM velocity field with the present data. However, the sensitivity is within an order of magnitude of that necessary to detect the predicted thermal SZ effect from the Lyα forest. We are able to place a weak limit on the density in ionised baryons at $z = 3$ of $\Omega_{B,i} < 0.80$ at 95% confidence. Below we outline future developments which would make a direct detection possible.

5.2 Discussion

In the present paper, we have examined the relationship between Lyα forest absorption and the SZ effect in general, without the expectation that a detection of a correlation can be made from current data. In the future, the quality and size of datasets will increase, and it will become worthwhile to plan a strategy for the cross-correlation that makes the best use of the data. Two obvious improvements could be made in the future. In our illustrative comparison of WMAP and SDSS data we did not use the full angular or frequency information, both of which would help with the sensitivity of the test.

As we have seen that the thermal SZ effect offers the best hope for detection of the ionised baryons, making use of the spectral difference between the SZ decrement and the primary CMB signal will enable easier detection of the effect. One could imagine fitting the τ_{eff} -T correlation in different CMB frequency bands to do this. For example, in the work of Huffenberger et al. (2004), a method was derived for combining the WMAP channels in an optimal manner to remove the primary anisotropy, effects of noise and contaminating point sources, enabling the thermal SZ signature to be constrained directly. In this paper we have concerned ourselves with predictions for the Rayleigh Jeans part of the spectrum, which is reasonable given the large observational uncertainties in present data. We note that at higher frequencies the thermal SZ signal becomes positive (for example at 330 GHz the magnitude is the same as the Rayleigh Jeans signal but with the opposite sign). Bolometers tend to be more sensitive than radiometers at present, and they operate at frequencies > 100 GHz. These differences could be used profitably to increase the signal to noise of any detection. Also, with the WMAP data, we have limited our analysis to single pixels. Making use of the full spatial cross-correlation in our detection of the signal will be useful when CMB datasets with higher angular resolution become available. Another possibility could be to use wavelets to isolate the relevant physical scales in a future analysis (see e.g., Vielva et al. 2005).

One can ask whether emission from the QSOs themselves might create a signal, as the SED of QSOs in the microwave band is not well constrained (Perna & Di Matteo 2000, White & Majumdar 2004). Apart from the possible intrinsic microwave emission of QSOs, there will also be an intrinsic thermal SZ effect from galaxy clusters which host QSOs. Neither of these will necessarily bias any measurement of the Lyα -CMB correlation unless QSOs with more Lyα absorption in their spectra have more intrinsic microwave emission. This seems unlikely in the former case, although in the case of an SZ signal associated with clusters in which the QSOs lie one could argue that this is part of the signal that we are trying to measure. Otherwise, it could be removed if we so desire by not using the part of the spectrum closest to the QSO.

The method we have outlined in this paper is one way to potentially detect ionised baryons in the IGM at high redshift. In general, one would like to know if there are any other methods that can be used. At lower redshifts, for example ($z < 1$), the ionised baryons are mainly collisionally ionised, with such a low neutral fraction that they cannot be seen in the Lyα forest. Their higher temperature, however, means that this Warm Hot Intergalactic Medium (WHIM, see e.g., Cen et al. 1995, 1999, Davé et al 2001) can potentially be detected by looking for X-ray absorption (e.g., Fang et al. 2002) or emission (Yoshikawa et al. 2004, Fang et al. 2005) or perhaps in Lyα emission (e.g. Furlanetto et al. 2003, 2005). The thermal SZ signal at low redshifts is also one way to detect the WHIM. At higher redshifts and lower IGM temperatures considered in this paper however, the X-ray signal (see e.g., Croft et al. 2001) is not likely to be observable.

The overall y-distortion in the CMB spectrum from the hot IGM should eventually be detectable. Limits from the COBE FIRAS instrument (e.g., Mather et al. 1990) are $y < 2.5 \times 10^{-5}$ at 95% confidence, more than an order of magnitude above the mean y caused by the high-z IGM. However, separating out the contribution from the high z IGM will be difficult without a spatial correlation of the type we have proposed here. One could also use other tracers of the high z density field for a cross-correlation, such as Lyman-break galaxies, or QSOs themselves, although their connection to the IGM would be less easy to interpret.

Another interesting question to ask is how likely it is that we will be able to constrain the high z IGM velocity field, given that the kinetic SZ signal from the photoionised IGM is expected to be relatively important (Loeb 1996). Because of the possible +ve or -ve nature of the effect, depending on the velocity, we cannot use a mean signal, unlike the thermal SZ. By using an rms fluctuation as our statistic, we therefore need a noise level which is extremely low. Since the spectrum of the kSZ is the same as the CMB, the primary fluctuations become even more important sources of

noise than with the thermal effect. Given that the rms fluctuations on scales of 1 arcmin from the kSZ are predicted to be $\sim 5\mu K$ at $z = 2$, one would need the "noise" from primary anisotropies and other sources to be less than this in order to detect a signal.

The thermal SZ is more promising. Future experiments which will be useful for improving constraints on $\Omega_{b,I}$ include the Planck satellite mission[2], the Sunyaev Zel'dovich Array (SZA[3]), the Atacama Cosmology Telescope (ACT, see Kosowsky 2003), and the South Pole Telescope (SPT[4]). Given the expected noise characteristics and angular resolution/sky coverage of these instruments, we expect substantial improvements over the constraints derived using WMAP in this paper. We have seen in the WMAP case (Section 4) that we are limited both by the noise level ($\sim 60\mu K$ rms) and the resolution of the data. As an example, the ACT angular resolution is projected to be ~ 1 arcmin with an rms detector noise level of $\sim 2\mu K$ per pixel in the 145 GHz band. Even without allowing for the higher resolution or using the full angular cross-correlation information, one would therefore expect to extract the same level Lyα forest thermal SZ signal using $(60/2)^2$ fewer spectra (assuming the primary anisotropy can be filtered out in frequency space). The ACT signal will be lower by about 50% at 145 GHz than the Rayleigh Jeans prediction, but the other frequency bands can be used to increase the significance of the detection. In order to yield a 2-σ detection of Ω_b, using pixel-pdf statistics, as in this paper, we estimate that ~ 300 quasar Lyα forest spectra would be needed in the ACT survey area, assuming the BBN value of $\Omega_b h^2$ (0.019; Burles & Tytler 1998) Using angular cross-correlation information would increase the significance of the detection. The lack of overlap between the ACT fields and the SDSS would necessitate a southern quasar survey, although it should be borne in mind that only extremely low resolution spectra are needed.

We note that in our analysis we have assumed that the ratio of neutral to ionised hydrogen is that expected if the ionising background radiation field does not vary spatially in intensity. If there are coherent spatial fluctuations in the photoionisation rate (Γ in Equation 1) then the correlation between Lyα optical depth and CMB temperature decrement will be affected by an additional source of scatter. This is likely to be small, however with the spatial cross-correlation reduced by 5% or less (see e.g., Croft 2004) and could in principle be calibrated out using theoretical modelling in the manner of McDonald et al. 2005.

Finally, one can ask why it is important to try to detect the ionised component of the baryons at high redshift when the neutral hydrogen tracer has already been well measured (e.g., Rauch et al. 1997). One reason is that a detection would act as a consistency check and enable us to verify directly the baryon inventory at these redshifts. Also, at the moment, the best constraints on the baryon density in observed structures (if we set aside for the moment relatively indirect CMB and Big Bang Nucleosynthesis, BBN measurements e.g., Spergel et al. 2003, Walker et al. 1991) comes from looking at the mean absorption level in the Lyα for-

est (e.g., Rauch et al. 1997, Weinberg et al. 1997, Hui et al. 2002, Tytler et al. 2004). However, these measurements are degenerate with constraints on the ionising background radiation intensity J. Often, Ω_b from BBN or CMB is assumed and then the Lyα forest measurement is used to constrain the ionising radiation intensity (e.g., Kirkman et al. 2005). If we use actual measurements of J (from e.g., the proximity effect e.g., Scott et al. 2000) then constraints on Ω_b directly seen in the Lyα forest become weaker (J is only known to within roughly a factor of two). Measurements of the ionised baryon fraction such as those we propose may therefore become competitive.

REFERENCES

Abazajian, K., et al. 2005, Astron. J., 129, 1755

Bennett, C. L., Halpern, M., Hinshaw, G., Jarosik, N., Kogut, A., Limon, M., Meyer, S. S., Page, L., Spergel, D. N., Tucker, G. S., Wollack, E., Wright, E. L., Barnes, C., Greason, M. R., Hill, R. S., Komatsu, E., Nolta, M. R., Odegard, N., Peiris, H. V., Verde, L. & Weiland, J. L ., 2003, ApJS, 148,1

Bradley, E., 1982, *The Jackknife, the Bootstrap and other resampling plans*, Philadelphia: SIAM.

Burles, S., & Tytler, D., 1998, ApJ, 499, 699

Carlstrom, J.E., Holder, G. & Reese, E.D., 2002, ARA&A, 40, 643

Cen, R., Miralda-Escudé, J., Ostriker, J. P., & Rauch, M. 1994, ApJ, 437, L9

Cen, R, Kang, H., Ostriker, J. P., Ryu, D., 1994, ApJ, 451, 436

Croft, R.A.C., Weinberg, D.H., Katz, N., & Hernquist, L. 1998, ApJ, 495, 44

Croft, R. A. C. and Di Matteo, T. and Davé, R. and Hernquist, L. and Katz, N. and Fardal, M. A. and Weinberg, D. H., 2001, ApJ, 557, 67

Croft, R.A.C., 2004, ApJ, 610, 642

da Silva, A. C., Barbosa, D., Liddle, A. R., Thomas, P. A., 2000, MNRAS, 317, 37

Davé, R., Hernquist, L., Katz, N., & Weinberg, D. H. 1999, ApJ, 511, 521

Davé, R., Cen, R., Ostriker, J. P., Bryan, G. L., Hernquist, L., Katz, N., Weinberg, D. H., Norman, M. L., O'Shea, B., 2001, ApJ, 552, 473

Fang, T., Marshall, H. L., Lee, J. C., Davis, D. S., Canizares, C. R, 2002, ApJ, 572, 127

Fang, T. and Croft, R. A. C. and Sanders, W. T. and Houck, J. and Davé, R. and Katz, N. and Weinberg, D. H. and Hernquist, L., 2005, ApJ, 623, 612

---

[2] http://planck.esa.int
[3] http://astro.uchicago.edu/sza
[4] http://astro.uchicago.edu/spt

Furlanetto, S., Schaye, J., Springel, V. & Hernquist, L. 2003, ApJ, 599, L1

Furlanetto, S., Schaye, J., Springel, V. & Hernquist, L. 2005, ApJ, 622, 7

Gardner, J.P., Katz, N., Hernquist, L., & Weinberg, D. 2003, ApJ, 587, 1

Gnedin, N.Y. & Hui, L., 1998, MNRAS, 296, 44

Gunn, J.E. & Peterson, B.A., 1965, ApJ, 142, 1633

Haardt, F. & Madau, P., 1996, ApJ, 461,20

Hernquist, L., Katz, N., Weinberg, D. & Miralda-Escudé, J. 1996, ApJ, 457, L51

Huffenberger, K. M., Seljak, U. & Makarov, A., 2004, PRD, 70, 063002

Hui, L., Burles, S., Seljak, U., Rutledge, R. E., Magnier, E., Tytler, D. 2001, ApJ, 552, 15

Hui, L., Haiman, Z., Zaldarriaga, M., Alexander, T., 2002, ApJ, 564, 525

Katz, N., Weinberg, D.H., & Hernquist, L., & Miralda-Escudé, J., 1996a, ApJ, 457, L57

Katz, N., Weinberg, D.H., & Hernquist, L., 1996b, ApJS, 105, 19

Kirkman, D., Tytler, D., Suzuki, N., Melis, C., Hollywood, S., James, K., So, G., Lubin, D., Jena, T., Norman, M. L.; Paschos, P., 2005, MNRAS, 360, 1373

Kosowsky, A., 2003, New Astronomy Review, 47, 939.

Kuo, C. L., Ade, P. A. R., Bock, J. J., Cantalupo, C., Daub, M. D., Goldstein, J., Holzapfel, W. L., Lange, A. E., Lueker, M., Newcomb, M., Peterson, J. B., Ruhl, J., Runyan, M. C., Torbet, E., 2004, ApJ, 600, 32

Loeb, A., 1996, ApJ, 471, L1

Mather, J. C. and Cheng, E. S. and Eplee, R. E. and Isaacman, R. B. and Meyer, S. S. and Shafer, R. A. and Weiss, R. and Wright, E. L. and Bennett, C. L. and Boggess, N. W. and Dwek, E. and Gulkis, S. and Hauser, M. G. and Janssen, M. and Kelsall, T. and Lubin, P. M. and Moseley, S. H. and Murdock, T. L. and Silverberg, R. F. and Smoot, G. F. and Wilkinson, D. T., 1990, ApJ, 354, L37

McDonald, P., Miralda-Escudé, J., Rauch, M., Sargent, W. L. W., Barlow, T. A., Cen, R., 2001, ApJ, 562, 52

McDonald, P., Seljak, U., Burles, S., Schlegel, D.J., Weinberg, D.H., Shih, D., Schaye, J., Schneider, D.P., Brinkmann, J., Brunner, R.J., Fukugita, M., 2004, ApJ, submitted [astro-ph/0405013]

McDonald, P., Seljak, U., Cen, R., Bode, P., & Ostriker, J. P., 2005, MNRAS, 360, 1471

McQuinn, M., Furlanetto, S.R, Hernquist, L., Zahn, O., & Zaldarriaga, M. 2005, ApJ, in press [astro-ph/0504189]

Nagamine, K., Cen, R., Hernquist, L., Ostriker, J. P., Springel, V., 2005, ApJ, 627, 608

Ostriker, J.P, & Vishniac, E.T., 1986, ApJ, L51

Perna, R., & Di Matteo, T., 2000, ApJ, 542, 68

Petitjean, P., Muecket, J.P., & Kates, R., 1995, A & A, 295, 9

Rauch, M., 1998, ARA&A, 36, 267

Rauch, M., Miralda-Escudé, J., Sargent, W. L. W., Barlow, T. A., Weinberg, D. H., Hernquist, L., Katz, N., Cen, R., & Ostriker, J. P., 1997, ApJ, 489, 7

Schaefer, B.M., Pfrommer, C., Hell, R. & Bartelmann, M., 2004, MNRAS, submitted [astro-ph/0407090]

Schaye, J., Theuns, Tom, Rauch, M., Efstathiou, G. & Sargent, W. L. W., 2000, MNRAS, 318, 817

Schaye, J., Aguirre, A., Kim, T.-S., Theuns, T., Rauch, M.,

Sargent, W. L. W., 2004, ApJ, 596, 768

Scott, J., Bechtold, J., Dobrzycki, A., & Kulkarni, V., 2000, ApJS, 130, 67

Spergel, D. N., Verde, L., Peiris, H. V., Komatsu, E., Nolta, M. R., Bennett, C. L., Halpern, M., Hinshaw, G., Jarosik, N., Kogut, A., Limon, M., Meyer, S. S., Page, L., Tucker, G. S., Weiland, J. L., Wollack, E.& Wright, E. L., 2003, ApJS, 148, 175

Springel, V., 2005, MNRAS, submitted [astro-ph/0505010]

Springel, V., White, M., & Hernquist, L, 2001, ApJ, 549, 681

Springel, V., White, M., & Hernquist, L, 2002, ApJ, 579, 16

Springel, V. & Hernquist, L, 2002, MNRAS, 333, 649

Springel, V. & Hernquist, L, 2003a, MNRAS, 339, 289

Springel, V. & Hernquist, L, 2003b, MNRAS, 339, 312

Springel, V., Yoshida, N., & White, S.D.M., 2001, New Astronomy, 6, 79

Sunyaev, R. A., & Zel'dovich, Ya. B. 1972, CoASP, 4, 173

Sunyaev, R. A., & Zel'dovich, Ya. B. 1980, ARA&A, 18, 537

Suzuki, N., Tytler, D., Kirkman, D., O'Meara, J. M., Lubin, D., 2005, ApJ, 618,592

Tegmark, M., et al. , 2004, Phys. Rev. D, 69, 3501

Tytler, D., Kirkman, D., O'Meara, J. M., Suzuki, N., Orin, A., Lubin, D., Paschos, P., Jena, T., Lin, W.-C., Norman, M. L., Meiksin, A., 2004, ApJ, 617, 1

Vielva, P., Martínez-González, E., Tucci, M., 2005, MN-RAS, *in press*, astro-ph/0408252

Wadsley, J. W., & Bond, J.R. 1997, in Proc. 12th Kingston Conference, Computational Astrophysics, eds. D. Clarke & M. West, ASP Conference Series 123, (San Francisco: ASP), astro-ph/9612148

Walker, T. P., Steigman, G., Kang, H., Schramm, D. M., Olive, K. A., 1991, ApJ, 376, 51

Weinberg, D. H., Miralda-Escudé, J., Hernquist, L., Katz, N., 1997, ApJ, 490, 564

White, M. & Majumdar, S., 2004, 602, 565

Yoshida, N., Furlanetto, S., & Hernquist, L., 2005, ApJ, 618, L91

Yoshikawa, K. and Dolag, K. and Suto, Y. and Sasaki, S. and Yamasaki, N. Y. and Ohashi, T. and Mitsuda, K. and Tawara, Y. and Fujimoto, R. and Furusho, T. and Furuzawa, A. and Ishida, M. and Ishisaki, Y. and Takei, Y., 2004, PASJ, 56, 939

Zhang, Y., Anninos, P., & Norman, M. L. 1995, ApJ, 453, L57